University of Groningen

Studies on the growth of voids in amorphous glassy polymers

Steenbrink, A.C.; van der Giessen, E.; Wu, P.D.

IMPORTANT NOTE: You are advised to consult the publisher's version (publisher's PDF) if you wish to cite from it. Please check the document version below.

Document Version
Publisher's PDF, also known as Version of record

Link to publication in University of Groningen/UMCG research database

Studies on the growth of voids in amorphous glassy polymers

A. C. STEENBRINK, E. VAN DER GIESSEN
Laboratory for Engineering Mechanics, Delft University of Technology, Delft, The Netherlands

P. D. WU
Faculté des Sciences Appliquées, Université de Sherbrooke, Sherbrooke, Canada
Email: E. Vander Gessen@wlmt.tudelft.nl

Numerical studies are presented of the localized deformations around voids in amorphous glassy polymers. This problem is relevant for polymer–rubber blends once cavitation has taken place inside the rubber particles. The studies are based on detailed finite element analyses of axisymmetric or planar cell models, featuring large local strains and recent material models that describe time-dependent yield, followed by intrinsic softening and subsequent strain hardening due to molecular orientation. The results show that plasticity around the void occurs by a combination of two types of shear bands, which we refer to as wing and dog-ear bands, respectively. Growth of the void occurs by propagation of the shear bands, which is driven by orientational hardening. Also discussed is the evolution of the local hydrostatic stress distribution between voids during growth, in view of possible craze initiation. © *1998 Kluwer Academic Publishers*

1. Introduction

Voids play a dominant role in the inelastic behaviour of amorphous polymers through, at least, two well-known mechanisms. First of all, crazing starts and propagates with the initiation and growth of voids [1, 2]. Even though crazing usually tends to lead to rather brittle fracture, void initiation and growth involve intense local plastic flow. Secondly, voids are a necessary step in the toughening mechanism in polymer–rubber blends [3, 4]. In the latter case, the voids are due to cavitation of the rubber particles, either internally or by debonding. The formation of voids facilitates plastic deformation in the glassy matrix, which then increases energy dissipation so as to contribute to enhancing the fracture toughness.

This toughening mechanism has been exploited for many years to produce blends on the basis of amorphous (but also semi-crystalline) polymers, with rubber volume fractions typically ranging from 20%–40% and particle sizes in the range of 0.1–10 μm. Well-known examples of amorphous blends are high-impact polystyrene (HIPS) and acrylonitrile–butadiene–styrene (ABS). Owing to many experimental studies, there is a quite elaborate, general picture of the toughening mechanisms, but many details are not understood well, especially not quantitatively.

Because of the importance of voids involving or during plastic deformation in amorphous polymers, the behaviour of voided materials has been intensively studied both experimentally and theoretically. Focus-

ing here on the theoretical studies, continuum mechanics modelling has revealed the deformations around voids in purely elastic materials (e.g. [5, 6]) and, much more recently, in elastic–plastic materials (e.g. [7–10]). These studies, when relating to blends, assumed that after cavitation of the rubber particles the rubber has no effect on the subsequent deformations in the matrix (provided that the rubber modulus is sufficiently low), so that the blend is replaced with a porous, pure matrix material with a void volume fraction equal to the initial rubber volume fraction. The finite element studies [8, 9] are mainly based on planar cell models containing a single void, but an axisymmetric model was also briefly considered [9].

The studies on void growth in polymers referenced above have used very simplistic, purely phenomenological material models available at the time. Meanwhile, considerable progress has been made in the fully three-dimensional, elastic–viscoplastic constitutive models for amorphous glassy polymers. Developments by Boyce and co-workers [11, 12] and subsequent modifications [13] have led to a constitutive model incorporating rate- and temperature-dependent plastic flow ("shear yielding"), including softening and subsequent strain hardening, that is partly based and partly motivated by the underlying physical mechanisms. This constitutive model was adopted recently [14, 15] in cell model studies of a voided amorphous polymer. These studies predicted a rather complex phenomenology of plastic deformations

around the void, which is controlled by the initiation and propagation of shear bands. The latter process is governed by the typical features of intrinsic softening and progressive strain hardening.

The objective of the present work was to explore further the growth of voids by plastic flow in propagating shear bands, under different states of applied stress and for different void volume fractions. In addition to the axisymmetric model [15], we also considered an analogous planar model, and the differences in predictions for different values of the material parameters are discussed. A study of how the hydrostatic stress field in the matrix material is affected by the localized plastic flow was also made. Although crazing itself is not modelled, this pertains to questions as to when and where the critical stress is attained for craze initiation.

2. The unit cell models

The studies were carried out in terms of unit cell models either with axial symmetries or in plane strain conditions. As illustrated in Fig. 1a, the axisymmetric cell model is an approximation for a material with a spatial distribution of spherical voids subjected to a macroscopic principal stress state $\Sigma_1, \Sigma_2, \Sigma_3 = \Sigma_1$ in the (x_1, x_2, x_3)-coordinate system. The voids are assumed to be arranged in a hexagonal closed packing in planes normal to and stacked in the x_2-direction. Each hexagonal cell around voids behaves exactly the same. All faces of the cell remain flat with zero shear tractions. The normal tractions on the hexagonal faces are averaged out to Σ_2, while those on the lateral faces are subject to the same stress Σ_1 because of cylindrical symmetry of the stress state about the x_2-axis. The cylindrical cell is an approximation of the hexagonal cell for computational reasons. In the undeformed state, the voids have a radius a_0, the half-spacing between planes of voids is h_0 and the hexagonal region around each void is replaced with a circle of radius b_0. The initial value of the void volume fraction f is $f_0 = \frac{2}{3}a_0^3 (b_0^2 h_0)$.

Also, a planar version of this cell model was employed. Such a unit cell represents a material with a doubly periodic packing of cylindrical voids with axes along x_3 subjected to macroscopic principal stresses along the coordinate axes. The initial void radius and the half-spacings between voids in x_1- and x_2-directions are denoted by a_0, b_0 and h_0 respectively, as in the axisymmetric model. The initial value of the void area fraction, f, in this case is $f_0 = (\pi/4)a_0^2(b_0 h_0)$. In these planar analyses it is assumed that Σ_3 is such that plane strain conditions prevail, i.e., the associated strain-rate $\dot{E}_3 = 0$.

Thus, the cross-section of both cell model versions is the same, as illustrated in Fig. 1b. Its boundaries remain straight during the deformation process and free of any shear tractions. Due to symmetry, only the shaded region of each cell needs to be analysed. The loading is assumed to be displacement controlled by prescribing the velocity $\dot{U}_2$ at the cell top, so that the applied strain-rate $\dot{E}_2 = \dot{U}_2/h$ is constant in time (h is the deformed height of the cell, $h = h_0 + U_2$). The transverse rate of deformation $\dot{E}_1 = U_1/b$ is prescribed at each instant by prescribing the velocity $\dot{U}_1$ along the lateral sides ($b = b_0 + U_1$ is the current
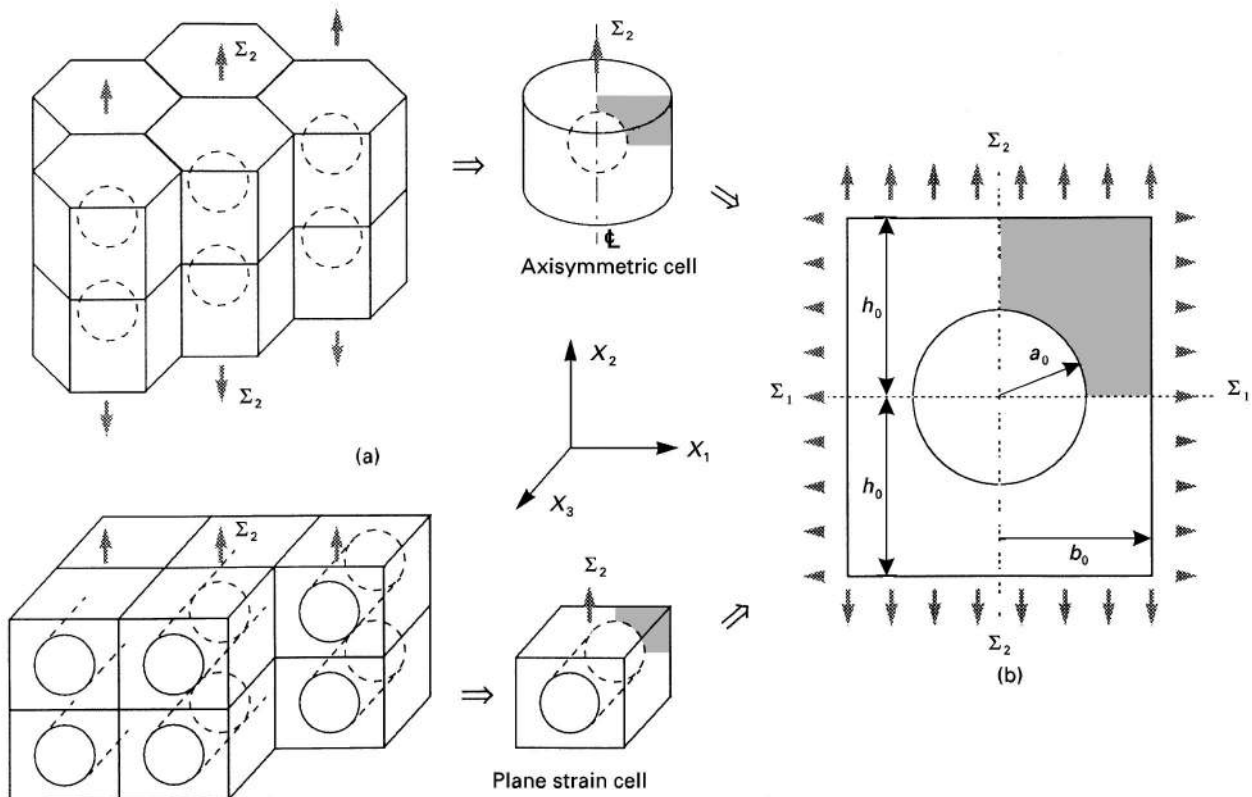

Figure 1 (a) Motivations of the axisymmetric unit cell model for a periodic material with spherical voids, and the planar cell model for a periodic material with cylindrical voids. (b) Geometry of unit cells; only the shaded area is analysed by virtue of symmetry.

radius/width of the cell), such that the stress ratio Σ_1/Σ_2 is kept at a constant value during the deformation process. This ensures that the overall stress triaxiality ratio Σ_m/Σ_e retains a constant, predetermined value at all stages of process. Here, Σ_m is the macroscopic mean (or hydrostatic) stress and Σ_e is the macroscopic Mises stress, which are, in general, defined in terms of the principal stresses Σ_i as

$$\Sigma_m = \tfrac{1}{3} \sum_{k=1}^{3} \Sigma_k \qquad (1a)$$

$$\Sigma_e = (\tfrac{3}{2} \Sigma_i' \Sigma_i')^{1/2} \qquad (1b)$$

$$\Sigma_i' = \Sigma_i - \Sigma_m \qquad (1c)$$

(the prime denotes the deviator, and summation over repeated indices is implied). For the two loading cases considered here, these expressions become:

Axisymmetric

$$\Sigma_e = |\Sigma_2 - \Sigma_1| \qquad (2a)$$

$$\Sigma_m = \tfrac{1}{3}(\Sigma_2 + 2\Sigma_1) \qquad (2b)$$

Plane strain

$$\Sigma_e = \tfrac{1}{2}\sqrt{3}\,|\Sigma_2 - \Sigma_1| \qquad (3a)$$

$$\Sigma_m = \tfrac{1}{2}(\Sigma_2 + \Sigma_1) \qquad (3b)$$

The expressions for axisymmetric conditions are exact; those for plane strain conditions are approximations, derived for an unvoided, incompressible material.

The macroscopic state of deformation at each instant is specified in terms of the principal logarithmic strains $E_2 = \ln(1 + U_2/h_0)$ and $E_1 = \ln(b/b_0)$ in the planes of the cells ($E_3 = E_1$ for the axisymmetric case; $E_3 = 0$ for the plane strain model). For future reference, we introduce the overall effective, Mises-like strain, E_e, as a measure of the macroscopic distortion. In general, this is defined as

$$E_e = (\tfrac{2}{3} E_i E_i)^{1/2}$$

analogous to the Mises stress in Equation 1; more specifically here:

Axisymmetric

$$E_e = \tfrac{2}{3}|E_2 - E_1| \qquad (4)$$

Plane strain

$$E_e = \tfrac{2}{3}(E_2^2 - E_2 E_1 + E_1^2)^{1/2} \qquad (5)$$

Also for future reference, we define a macroscopic shear rate, $\dot{\Gamma}$, which represents the applied shear strain rate if there were no voids present:

Plain strain

$$\dot{\Gamma} = \frac{1}{\sqrt{2}}\,\dot{E}_2 \qquad (6a)$$

Axisymmetric

$$\dot{\Gamma} = \sqrt{\frac{3}{2}}\,\dot{E}_2 \qquad (6b)$$

It is noted that the only length scales involved in the model are the cell dimensions h_0, b_0 and the void

radius a_0; there is no intrinsic, material length scale other than these morphological parameters. Thus, the solution depends only on their ratios, namely a_0/b_0 and b_0/h_0. We shall confine attention to packings such that $h_0 = b_0$ so that the dependence of the results on the morphology is only through the ratio a_0/b_0 or equivalently through the initial void volume/area fraction, f_0.

3. Material model

The material model accounts for rate-dependent shear yielding, the intrinsic softening that immediately follows yield in amorphous polymers and the subsequent strain hardening due to the stretching of the entanglement network. The model closely follows the original ideas put forward in one dimension by Haward and Thackray [16] in which the strain hardening is represented by a Langevin spring in parallel to a yielding element. The first formulation in terms of a fully three-dimensional theory has been given by Boyce et al. [11]. We here employ a slightly modified version of that theory developed elsewhere [13].

Rate-dependent yielding is taken to be described by the expression

$$\dot{\gamma}^p = \dot{\gamma}_0 \exp\left[-\frac{As_0}{T}\left(1 - \left(\frac{\tau}{s_0}\right)^{5/6} \right) \right] \qquad (7)$$

derived by Argon [17] for the plastic shear-rate, $\dot{\gamma}^p$, as a function of the driving shear stress, τ. Here, $\dot{\gamma}_0$ is a pre-exponential factor, A is a material parameter that is proportional to the activation volume, T is the absolute temperature, and s_0 is the athermal shear strength. Boyce et al. [11] extended this expression in a phenomenological way to include the effect of pressure and strain softening. They use $s + \alpha p$ instead of s_0 where p is the pressure and α is a pressure-dependence coefficient. Furthermore, s is assumed to evolve with plastic straining from the initial value s_0 to a steady-state value s_{ss}, via

$$\dot{s} = h(1 - s/s_{ss})\dot{\gamma}^p \qquad (8)$$

to incorporate a phenomenological description of softening. The rate of softening is governed by the material parameter h.

The driving shear stress, τ, in the flow rule (Equation 7), is determined in the three-dimensional theory from

$$\tau = (\tfrac{1}{2}\bar{\sigma}_{ij}'\bar{\sigma}_{ij}')^{1/2} \qquad (9a)$$

$$\bar{\sigma}_{ij} = \sigma_{ij} - b_{ij} \qquad (9b)$$

$$\bar{\sigma}_{ij}' = \bar{\sigma}_{ij} - \tfrac{1}{3}\bar{\sigma}_{kk}\delta_{ij} \qquad (9c)$$

where σ_{ij} is the local stress tensor and b_{ij} is the back stress ($i, j \in 1, 2, 3$ and δ_{ij} is the Kronecker delta). The back stress is an internal stress associated with the stretching of the entanglement network upon continued plastic deformation. Following the suggestion

by Haward and Thackray [16], this back stress is modelled using non-Gaussian network theory. Thus, its principal components, b_i, have the same directions as the plastic stretch, and are direct functions of the corresponding principal plastic stretches, λ_i. It was shown by Wu and Van der Giessen [13] that the predictions of the full (or random) network theory could be captured accurately in terms of a simple combination of the classical three-chain network description and the Arruda–Boyce [12] eight-chain model

$$b_i = (1 - \rho)\, b_i^{3-\mathrm{ch}} + \rho b_i^{8-\mathrm{ch}} \qquad (10)$$

with ρ being determined by the maximum plastic stretch $\bar{\lambda} = \max(\lambda_1, \lambda_2, \lambda_3)$ through $\rho = 0.85\bar{\lambda}/N^{1/2}$. Here, N is a statistical network parameter, which gives the average number of links between entanglements (or cross-links in a rubber) and thus determines the limit stretch, $\lambda_{\max}$, of a molecular chain as $\lambda_{\max} = N^{1/2}$. The principal back stress components $b_i^{3-\mathrm{ch}}$ and $b_i^{8-\mathrm{ch}}$ are given by

$$b_i^{3-\mathrm{ch}} = \frac{1}{3} C^{\mathrm{R}} N^{1/2} \lambda_i \mathscr{L}^{-1}\left(\frac{\lambda_i}{\sqrt{N}}\right) \qquad (11)$$

$$b_i^{8-\mathrm{ch}} = \frac{1}{3} C^{\mathrm{R}} N^{1/2} \frac{\lambda_i^2}{\lambda_c} \mathscr{L}^{-1}\left(\frac{\lambda_c}{\sqrt{I}}\right) \qquad (12a)$$

$$\lambda_c^2 = \frac{1}{3} \sum_{j=1}^{3} \lambda_j^2 \qquad (12b)$$

where $\mathscr{L}^{-1}$ is the inverse of the Langevin function $\mathscr{L}(\beta) = \coth\beta - 1/\beta$. The material parameter C^{R} is termed the hardening modulus (in rubber elasticity, it is the shear rubbery modulus). When the value of either $\bar{\lambda}$ or λ_c approaches $\lambda_{\max}$, the hardening rate increases dramatically, thereby suppressing effectively all further plastic flow. Hence, the network locks. Therefore, for monotonic loading conditions, when either λ_i or λ_c exceeds the value $0.99\,\lambda_{\max}$, the network is "locked" and further viscoplastic flow is suppressed.

For further details on the constitutive model, readers are referred to other papers, [13, 18, 15]. We only note that the actual implementation of this model into a finite strain, finite element code to solve, for example, the void growth problem addressed above, requires special care in order to keep the computation numerically stable. When this is properly done, the material model has been shown to be able, under various deformation conditions, to describe the initiation of shear bands and their subsequent propagation typical for amorphous glassy polymers (e.g. [18]).

Most computations to be reported on here have been carried out for the following set of material parameters at room temperature ($T = 294\mathrm{K}$): $\nu = 0.3$, $E = 910$ MPa, $\dot{\gamma}_0 = 2 \times 10^{15} \mathrm{s}^{-1}$, $s_0 = 97$ MPa, $\alpha = 0.08$, $A = 240$ K MPa^{-1}, $h = 500$MPa, $s_{\mathrm{ss}} = 77$ MPa, $N = 6.3$ and $C^{\mathrm{R}} = 5.7$ MPa. These values are typical for polycarbonate (PC), but are otherwise representative for a range of glassy polymers. The elastic modulus, E, is chosen not to be equal to the initial
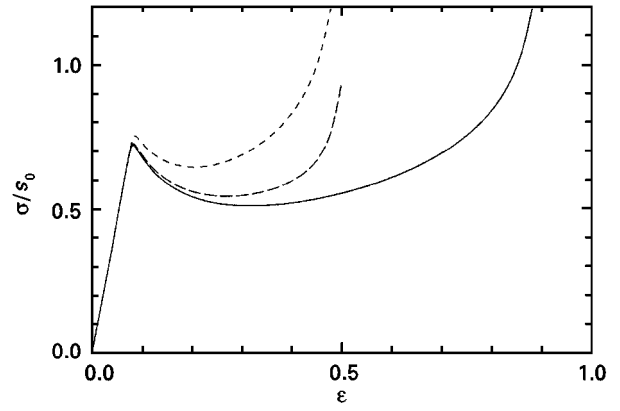

Figure 2 True stress, σ, versus logarithmic strain, ε, curves in uniaxial tension at a strain-rate of $\dot{\varepsilon} = 0.01\mathrm{s}^{-1}$ for the various sets of material parameters used in this paper. Values that are not explicitly mentioned are the same for all sets, and are given in the text. (——) $N = 6.3$, $C^{\mathrm{R}} = 5.7$ MPa, (- - -) $N = 2.8$, $C^{\mathrm{R}} = 5.7$ MPa, (– –) $N = 2.8$, $C^{\mathrm{R}} = 12.8$ MPa.

Young's modulus, because amorphous glassy polymers generally exhibit a small strain viscoelastic effect resulting in a nonlinear stress–strain response prior to yielding. Therefore, E is chosen to match a typical ratio between yield stress and yield strain in uniaxial tension (cf. [18]), which leads to a typical value of $E/s_o = 9.38$. To study briefly the effects of the softening and hardening characteristics, some results are shown for $N = 2.8$ and/or $C^{\mathrm{R}} = 12.8$ MPa. The uniaxial stress–strain curves for the matrix material corresponding these various parameter sets shown in Fig. 2 indicate that they cover a realistic range of ultimate strains and of stress drops upon softening. The effect of the softening rate, h, on void growth has been investigated elsewhere [15].

4. Axisymmetric versus planar deformations

Void growth computations are carried out in terms of the axisymmetric as well as the plane-strain model for two sizes of initial voids: $a_0/b_0 = 0.2$ or 0.5. The larger value is supposedly relevant for polymer–rubber blends in which the rubber particles have cavitated. For the axisymmetric model, the corresponding void volume fraction is around 10%, which is a reasonable value for the volume fraction of cavitated rubber particles in a blend at locations near, but not right at, the fracture plane. The smaller value of a_0/b_0 is considered in order to separate the effect of void interactions. The finite element mesh that is used for $a_0/b_0 = 0.2$ is shown in Fig. 3. A very fine mesh is needed around the void, especially near the equator in order to pick up the localized deformations that will be shown to develop for the materials under consideration. The macroscopically applied strain-rate $\dot{E}_2$ is equal to that used in Fig. 2.

4.1. Shear band patterns
Figs 4 and 5 show how the smaller voids, $a_0/b_0 = 0.2$, grow under two remote stress states, specified by
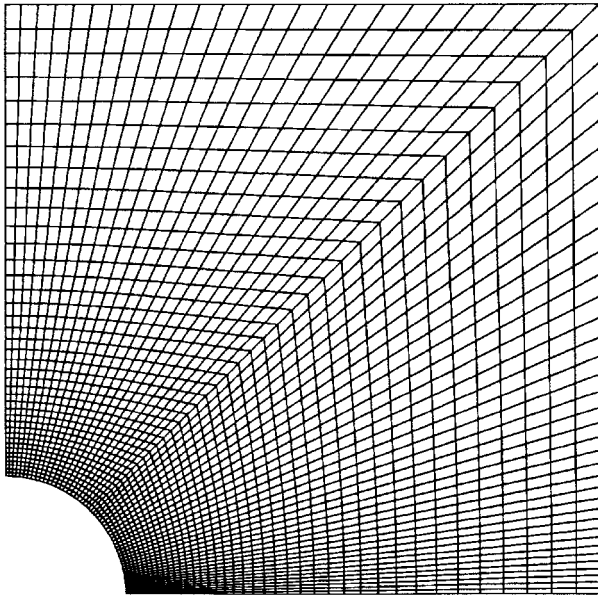
Figure 3 Finite element mesh of the shaded region in Fig. 1b used for the cases with $a_0/b_0 = 0.2$. The mesh used for $a_0/b_0 = 0.5$ has a similarly fine mesh around the void.

$\Sigma_1/\Sigma_2 = 0$ and 0.73, respectively. For each state of remote stress, results are shown for the planar model (a) and for the axisymmetric model (b). Under axisymmetry, $\Sigma_1/\Sigma_2 = 0$ implies remote uniaxial tension,

while $\Sigma_1/\Sigma_2 = 0.73$ corresponds to a remote stress triaxiality of $\Sigma_m/\Sigma_e = 3$ (cf. Equation 2), which is commonly considered to be representative for the state of stress ahead of a crack tip. For each state of stress and for both geometries, three snapshots of the instantaneous plastic zone are shown in Figs 4 and 5 at typical stages of the deformation process. These stages are marked in the computed macroscopic stress–strain curves for the various cases, shown in Fig. 6. The plastic zones are visualized in terms of contour plots of the current plastic shear rate, $\dot{\gamma}^p$, normalized by $\dot{\Gamma}$ from (Equation 6).

For the lower triaxiality, $\Sigma_1/\Sigma_2 = 0$, Fig. 4a shows that plasticity in the planar model starts with some highly concentrated plasticity near the equator of the void emanating in a well-defined shear band under $45°$. The thickness of this shear band is almost uniform and independent of the mesh size. In fact, previous numerical studies with the same material model of simpler problems like compression, have shown that the shear band thickness is controlled mainly by the softening and hardening characteristics of the material [18]. As the material inside this band continues to deform with continued overall strain, it first further softens and then strain hardens due to the stretching of the entanglement network, until the stress inside the band becomes large enough to trigger yield in neighbouring material. It is the continuous repetition of this
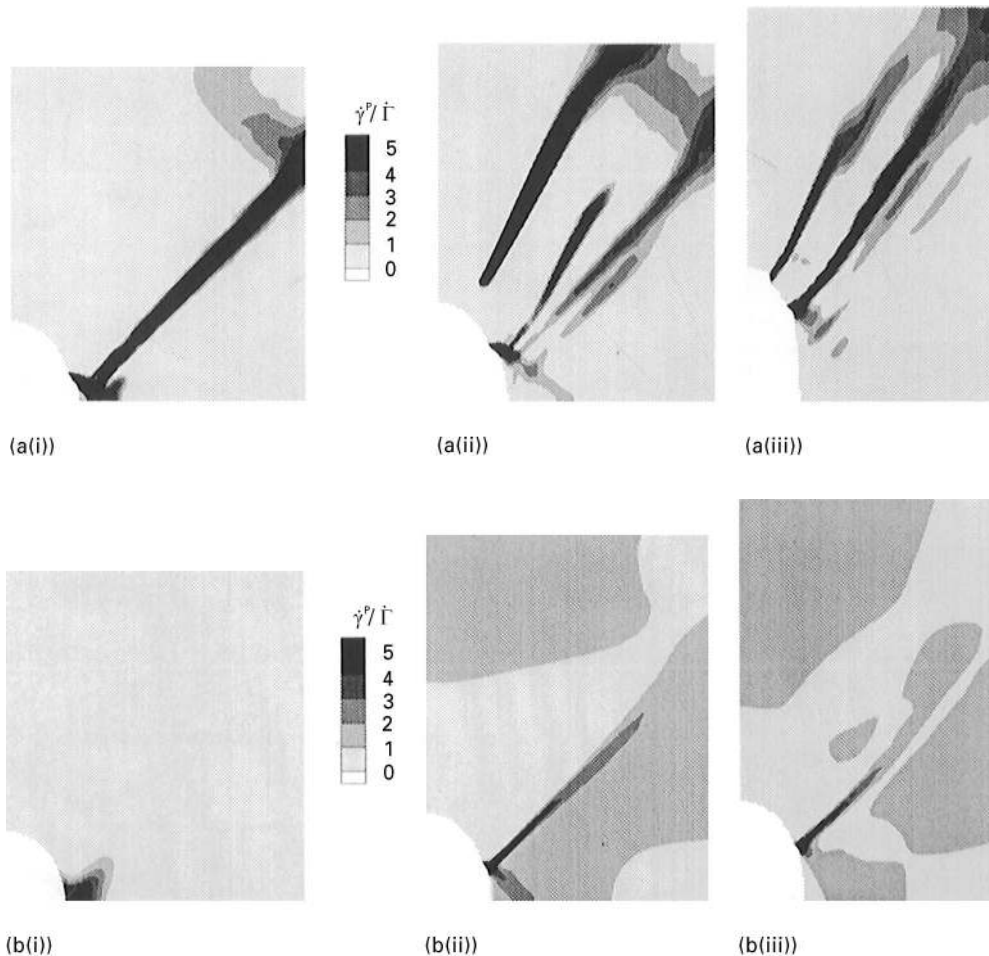

Figure 4 Distribution of the instantaneous plastic shear rate, $\dot{\gamma}^p$, for a material with $N = 6.3$, $C^R = 5.7$ MPa and with the initial void specified by $a_0/b_0 = 0.2$ for low triaxiality loading, $\Sigma_1/\Sigma_2 = 0$, under (a) plane strain, $E_e =$ (i) 0.072, (ii) 0.14, (iii) 0.25, and (b) axisymmetric conditions, $E_e =$ (i) 0.068, (ii) 0.16, (iii) 0.26. The corresponding stress–strain curve is shown in Fig. 6.
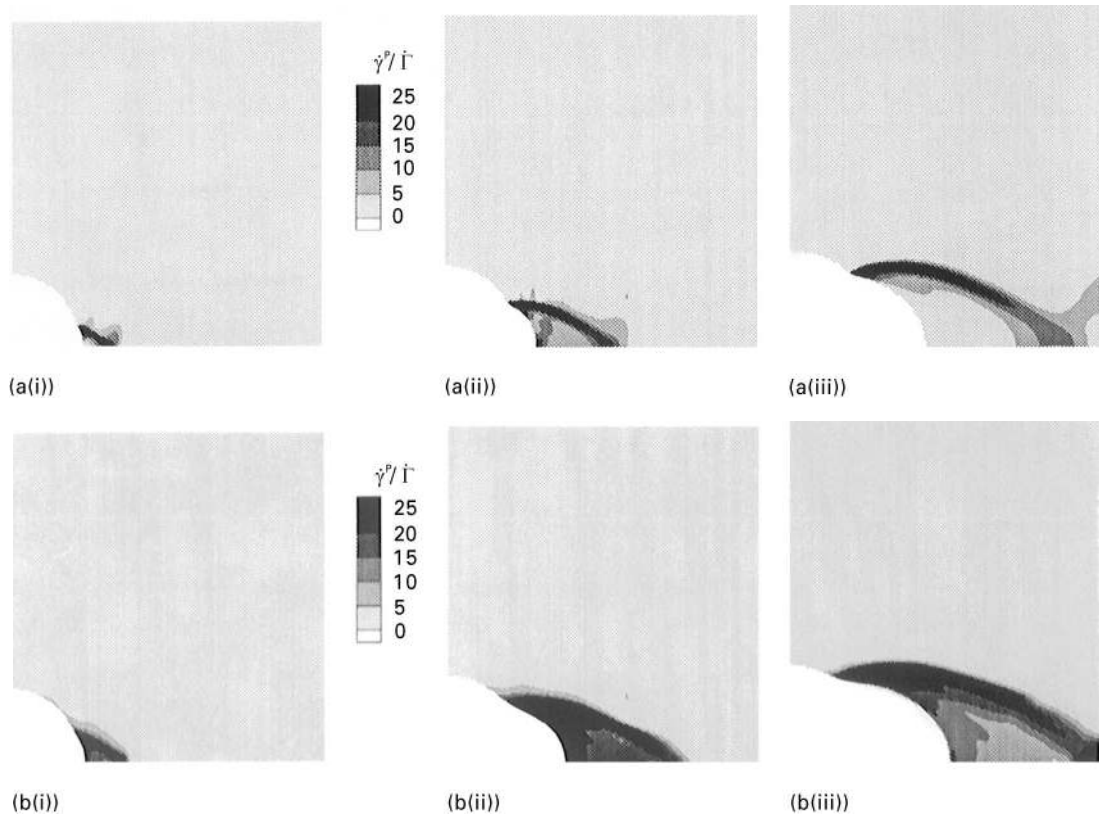
Figure 5 Distribution of the instantaneous plastic shear rate, $\dot{\gamma}^p$, for the same material as in Fig. 4 but for high triaxiality loading, $\Sigma_1/\Sigma_2 = 0.73$, under (a) plane strain, E_e = (i) 0.028, (ii) 0.043, (iii) 0.66, and (b) axisymmetric conditions, E_e (i) 0.026, (ii) 0.040, (iii) 0.060. The corresponding stress–strain curve is shown in Fig. 6.
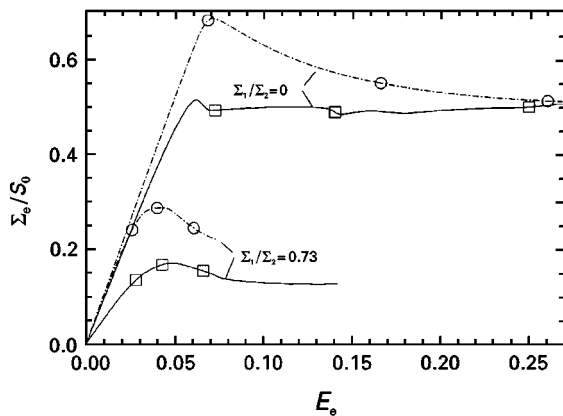

Figure 6 Macroscopic effective stress–effective strain response for material with $N = 6.3$, $C^R = 5.7$ MPa and with $a_0/b_0 = 0.2$. The symbols refer to the plots shown in Figs 4 and 5. ($\square$) Plane strain ($\bigcirc$) axisymmetric.

process that gives rise to propagation of the shear band, in the present case in the direction of loading. As a consequence of this shear band propagation, material appears to be drawn into the ligament between voids, and the void grows into a strongly prolate shape. In this plane strain case, the macroscopic stress remains virtually constant after macroscopic yield (see Fig. 6). Notice in Fig. 4a that more than one shear band can get triggered at larger strains. Also, we see some "reflections" of the shear bands in the top right-hand side of the quarter cell, which are in fact continuations of shear bands from the neighbouring cell.

This indicates that even for these relatively small voids, there is significant interaction with the next nearest voids.

In the axisymmetric model (see Fig. 4b), localization into shear bands is much less pronounced, but growth of the void is controlled again by propagation of shear bands. The shear bands are thinner than in the planar model and confined more to the neighbourhood of the void. This is an immediate consequence of the kinematics of localized shearing. In the axisymmetric model, a shear band is actually a cross-section of a conical plane; shearing along that plane requires circumferential straining for reasons of compatibility. As a consequence of this more confined shear banding, the macroscopic stress–strain curve is very different than that under plane strain conditions, and is, in fact, qualitatively similar to the homogenous stress–strain curve in Fig. 2.

The shear banding under higher stress triaxiality, $\Sigma_1/\Sigma_2 = 0.73$, shown in Fig. 5, is of a completely different nature. Rather than a shear band under 45°, we observe that plasticity starts with rather well-defined shear bands under roughly $-30°$ with the main loading direction, both in the planar and in the axisymmetric model. These shear bands appear well prior to macroscopic yielding (see Fig. 6), but localization into these shear bands intensifies at macroscopic yield and beyond, while the shear bands become slightly curved. In view of the shape of these shear bands we shall refer to them as "dog-ear" bands as compared to "wing" shear bands observed under low triaxiality in Fig. 4.

3168

Propagation of these dog-ear shear bands occurs in such a way that the shape of the band region remains the same, while it sweeps the entire ligament between voids with continued deformation. Due to this type of shear banding, the void grows into a markedly oblate shape, i.e., with the longest axis perpendicular to the maximal straining direction x_2.

Though limited, the models, which are in themselves planar or axisymmetric cell models, find their motivation in the expectation that either one of them, or both, capture some features of the behaviour of a real material in three dimensions with the same relative void size a_0/b_0 and subject to similar remote loading conditions. In view of the very fine meshes that are needed to resolve accurately the shear bands that occur, full three-dimensional void growth computations with the present material model pose enormous requirements on computational resources. However, the qualitative similarity between the results for the planar model versus those for the axisymmetric model in Figs 4 and 5, suggests that the real three-dimensional phenomena involved in void growth at the same remote stress triaxiality are similar. It is to be expected, however, that shear bands in three dimensions will prefer to take planar shapes, like in the present planar model, because this puts much milder requirements on deformation of the neighbouring material to ensure compatibility.

4.2. Void interaction

Figs 7 and 8 show how the above picture changes when $a_0/b_0 = 0.5$, i.e. when interactions between voids become more significant. Comparing the low triaxiality results in Fig. 7 with those for the smaller void in Fig. 4, it is seen that the larger void exhibits less tendency to grow into an oblate shape, especially in the planar model. This is caused by the fact that in this case, the shear band pattern changes after macroscopic yield (see Fig. 9). During the rather sharp drop in the macroscopic stress response right after macroscopic yield (see Fig. 7a for $E_e = 0.092$), one observes not a single wing-like shear band, but a number of such bands together with traces of two dog-ear shear bands. It is the latter type shear band that appears to survive at larger strains and tends to span across the entire remaining ligament. Under axisymmetric conditions (Fig. 7b) such dog-ear shear bands do not appear, but the wing-like shear bands are significantly weaker than for the smaller voids in Fig. 4b.

For the higher stress triaxiality in Fig. 8, we find only dog-ear shear bands, as for the smaller voids in Fig. 5, but the shear bands appear to be less intensive so that plastic deformation is more distributed over the matrix. In the planar model, in Fig. 8a, we again see traces of both families of shear bands appearing shortly after macroscopic yield.
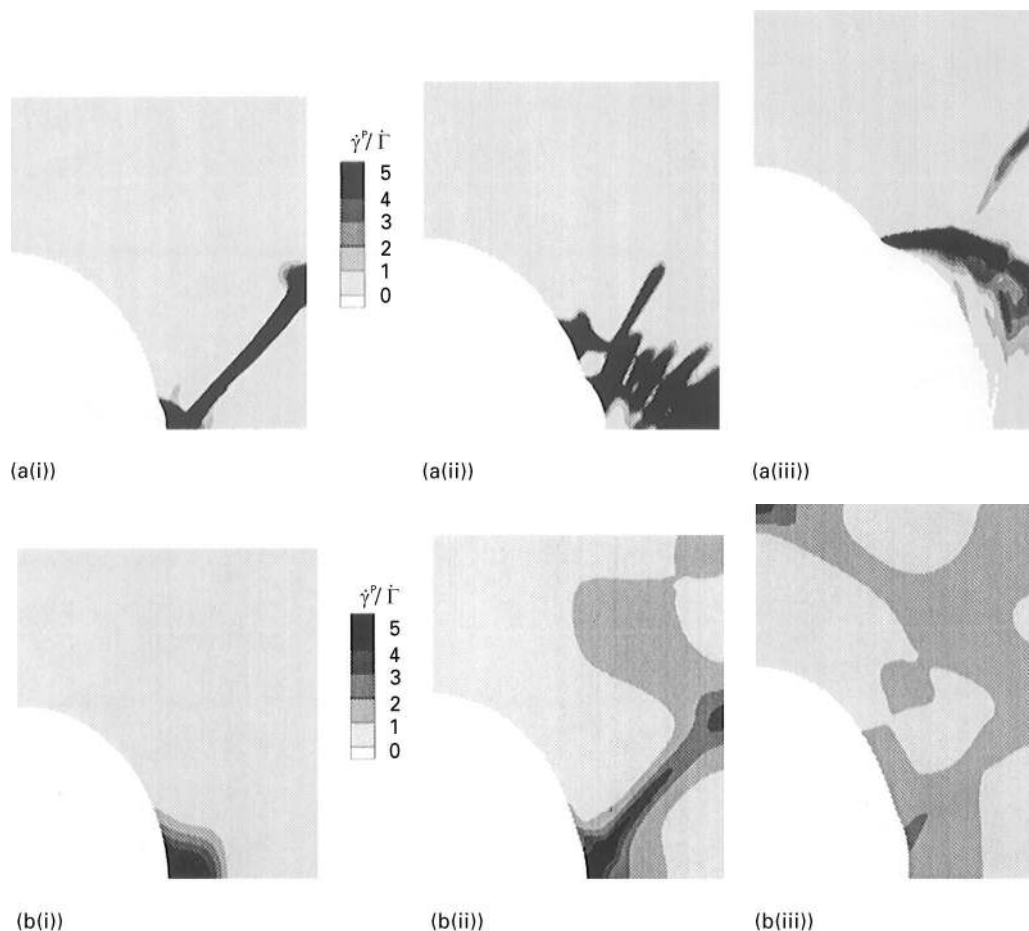

(a(i))   (a(ii))   (a(iii))

(b(i))   (b(ii))   (b(iii))

Figure 7 Distribution of the instantaneous plastic shear rate, $\dot{\gamma}^p$, for a material with $N = 6.3$, $C^R = 5.7$ MPa and with the initial void specified by $a_0/b_0 = 0.5$ for low triaxiality loading, $\Sigma_1/\Sigma_2 = 0$, under (a) plane strain, $E_e = $ (i) 0.064, (ii) 0.092, (iii) 0.21, and (b) axisymmetric conditions, $E_e = $ (i) 0.062, (ii) 0.10, (iii) 0.18. The corresponding stress–strain curve is shown in Fig. 9.
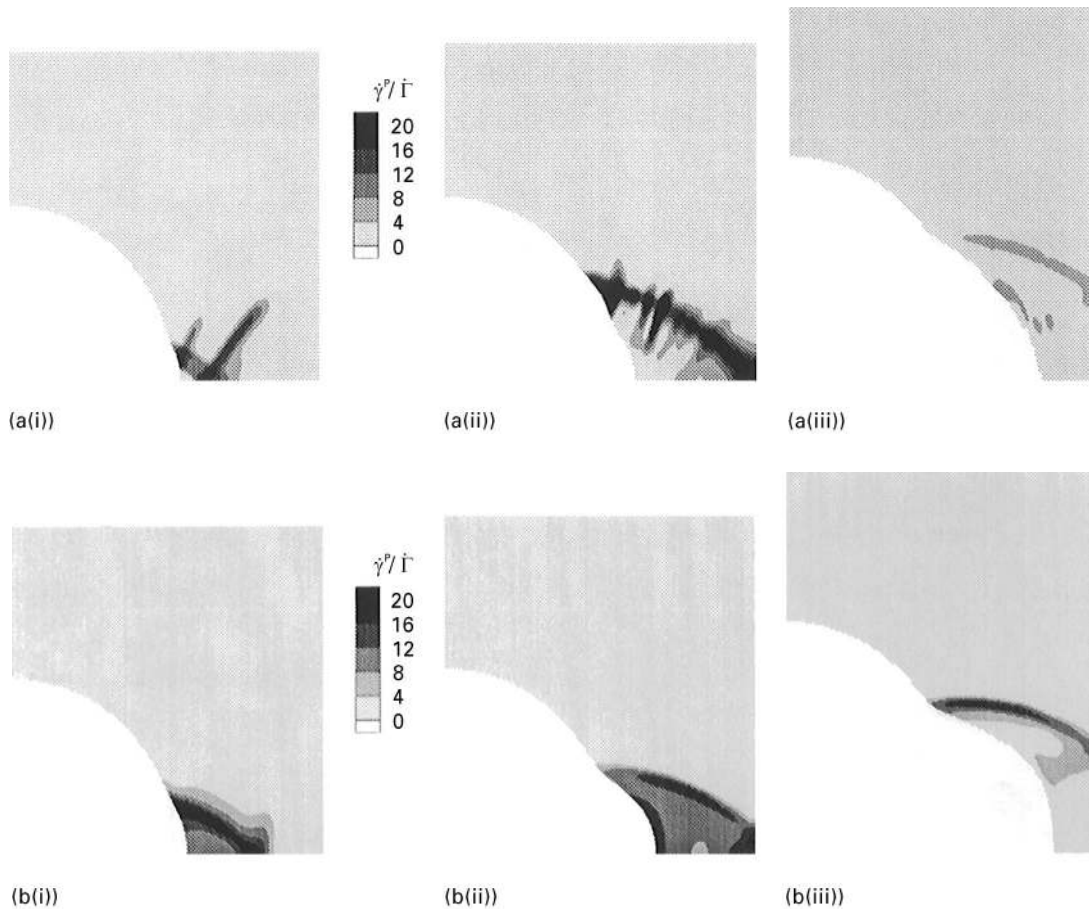
(a(i))   (a(ii))   (a(iii))

(b(i))   (b(ii))   (b(iii))

Figure 8 Distribution of the instantaneous plastic shear rate, $\dot{\gamma}^{\mathrm{p}}$, for the same material as in Fig. 7 but for high triaxiality loading, $\Sigma_1/\Sigma_2 = 0.73$, under (a) plane strain, $E_{\mathrm{e}} =$ (i) 0.036, (ii) 0.051, (iii) 0.13, and (b) axisymmetric conditions, $E_{\mathrm{e}} =$ (i) 0.029, (ii) 0.051, (iii) 0.13. The corresponding stress–strain curve is shown in Fig. 9.
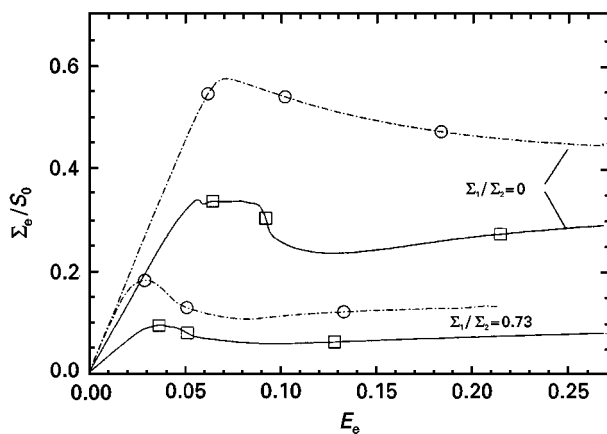

Figure 9 Macroscopic effective stress–effective strain response for material with $N = 6.3$, $C^{\mathrm{R}} = 5.7$ MPa and with $a_0/b_0 = 0.5$. The symbols refer to the plots shown in Figs 7 and 8. ($\square$) plane strain, ($\bigcirc$) axisymmetric.

4.3. Wing versus dog-ear shear bands

The following simple picture, illustrated in Fig. 10, emerges from the studies presented above and related previous work [14, 15]. Two types of shear band occur around voids in an amorphous glassy matrix: wing-like shear bands and dog-ear shaped bands. Wing-like bands are favoured at lower triaxialities, while dog-ear shear bands appear to be favoured at higher stress triaxialities and at higher concentrations of voids. At some stages of deformation, both families of shear bands are available, but this appears to be mainly a transition from one type to the other.

The wing-like shear bands originate at the equator of the void, and are oriented under approximately $45°$ relative to the maximal principal tensile stress direction. This initial location coincides with the location where plastic flow starts when Σ_2 is the maximal principal stress (as has been predicted long before from purely elastic analyses [5, 8, 9]). The orientation of about $45°$ is controlled primarily by the direction of maximum macroscopic shear stress. In the present analyses, this direction remains fixed during deformation, and the shear band retains its orientation when it propagates; but, in a more complex deformation history one should expect the shear band orientation to change as the maximum shear direction changes.

The dog-ear shear bands often appear as slightly curved shear bands, oriented roughly under $-30°$ with respect to the maximum macroscopic tensile stress. However, closer inspection shows that at the location where the shear band initiates from the void surface, it subtends an angle of again $45°$ with the local circumferential direction of the void surface. This indicates that the occurrence of these types of shear band is to some extent controlled by the void's circumferential stress state rather than by the macroscopic stress state. These shear bands are always formed after some
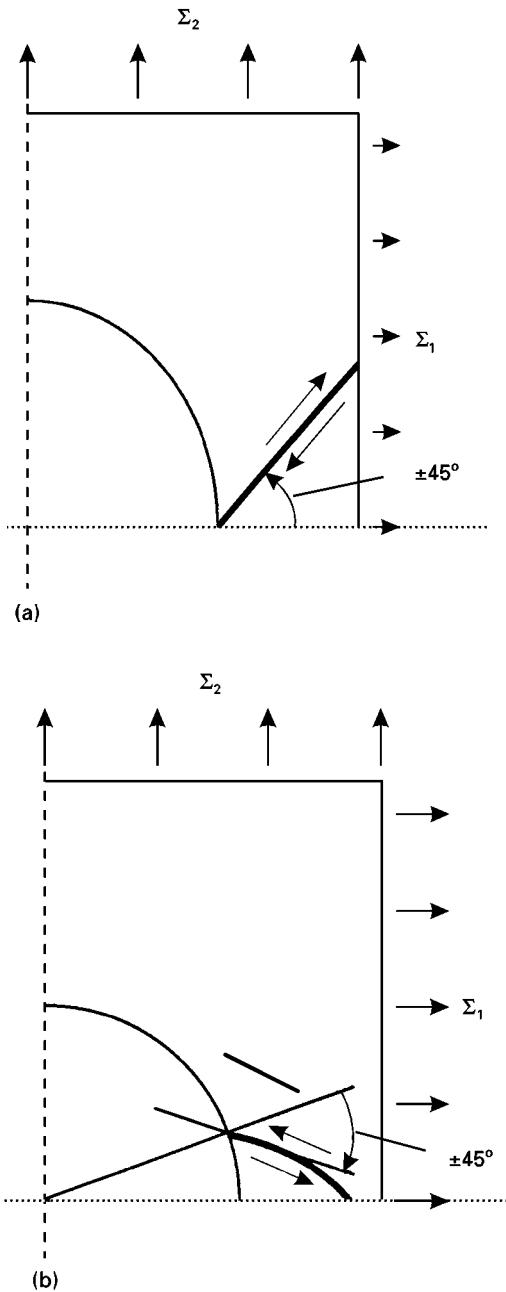
(a)

(b)

Figure 10 Schematic illustration of the two main types of shear bands that can form around voids in amorphous glassy polymers: (a) wing-like shear bands, (b) dog-ear shaped shear bands.

Figure 11 Applied strain, E_2, versus macroscopic lateral strain, E_1, for the material with $N = 6.3$, $C^{\mathrm{R}} = 5.7$ MPa and with $a_0/b_0 = 0.5$ (see also Fig. 9). The symbols refer to the plots shown in Figs 7 and 8. (□) plane strain, (○) axisymmetric.

amount of plasticity near the void equator, and therefore their presence can never be predicted from purely elastic considerations (in fact, Goodier's [5] analytical elastic solution for an isolated void, generalized to arbitrary remote stress triaxiality, as well as its plane strain counterpart predict the maximum circumferential stress to occur at the void equator too).

Especially for the relatively large voids considered in Figs 7 and 8, we have observed transitions from wing-like shear banding to dog-ear bands. This transition is reflected in the stress–strain curves as a rather sharp drop after macroscopic yield (see Fig. 9). Fig. 11 shows that the transition is also witnessed clearly in the response of the lateral macroscopic strain E_1 to the prescribed strain E_2 in the x_2-direction. For $\Sigma_1/\Sigma_2 = 0$, we find continuous lateral contraction in the axisymmetric cell, whereas for the planar model
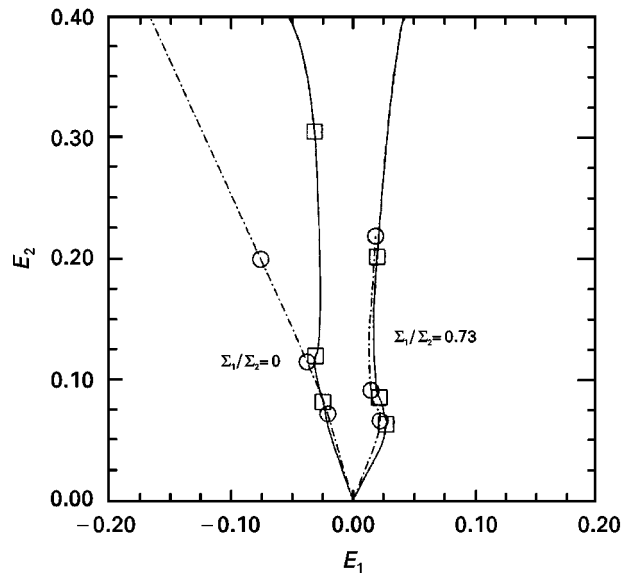
a marked kink is seen, at which continued straining is possible without significant lateral deformation. This kink $dE_1/dE_2 = 0$ coincides with the transition from a wing-like shear band at small strains into a dog-ear shaped band (see Fig. 9). A similar kink is observed at higher triaxiality, in both axisymmetric and planar models, but in these cases some lateral contraction follows this kink. This "snap back"-like phenomenon is associated with the release of elastic energy stored in the system when macroscopic softening takes place as the dog-ear shear band matures. Upon further straining, the contraction almost vanishes in the case where dog-ear bands had initiated until large applied strains; this is to be attributed to the drawing of the ligament between voids caused by the propagation of the shear band. These observations are confirmed by studies presented elsewhere [15].

It is emphasized that the occurrence of shear bands, and hence the competition between both types of shear bands, is determined by the local conditions of stress, strain-rate and state of deformation in the material. The conditions for shear banding in the present problem, where even the elastic field is non-homogeneous, cannot be established by simple analysis, but requires an accurate, detailed analysis of all governing field equations (which is done here through finite element discretization).

5. Effect of softening and hardening characteristics

The previous study [15] of void growth in amorphous polymers has briefly addressed the effect of the rate of intrinsic softening, h. In agreement with the results of other strain localization studies in these materials (e.g. [18]), it was found that the tendency for the formation of sharp shear bands decreases with decreasing h. Associated with this decrease, the amount of macroscopic softening after yield decreases, even
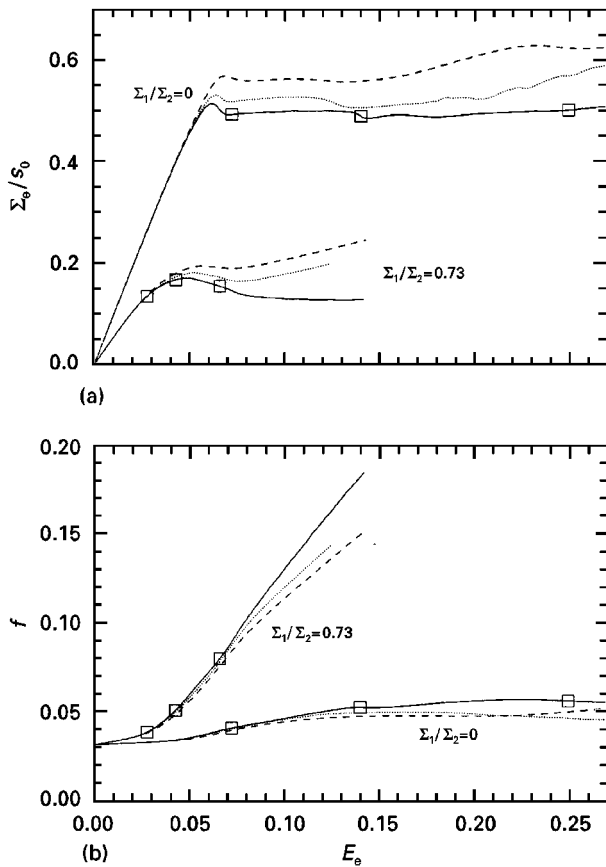
3171

Figure 12 Effect of C^R and N on (a) the macroscopic effective stress–effective strain response, (b) the void area fraction under plane strain conditions for a material with $a_0/b_0 = 0.2$. The symbols correspond to the plots in Figs 4 ($\Sigma_1/\Sigma_2 = 0$) and 5 ($\Sigma_1/\Sigma_2 = 0.73$). (——) $N = 6.3$, $C^R = 5.7$ MPa, (·· ··) $N = 2.8$, $C^R = 5.7$ MPa, (- - -) $N = 2.8$, $C^R = 12.8$ MPa.

though void growth itself may still provide "geometric softening" especially at higher stress triaxialities.

Here, we briefly investigate the effects of the parameters C^R and N that primarily determine the hardening characteristics of the material, but implicitly also affect the shear strength drop after yield, as demonstrated in Fig. 2. Even though the variations of N and C^R relative to the previously used values are seen to give rise to substantial changes in the response to homogeneous uniaxial tension (in unvoided material), the response of the voided material under uniaxial macroscopic tension ($\Sigma_1/\Sigma_2 = 0$) is found to be affected much less, even for the case with relatively small voids shown in Fig. 12a. The main effect appears to be that the macroscopic yield and the subsequent flow stress are elevated somewhat with increasing C^R or decreasing N; this is due to the fact that the maximum shear strain that is attainable inside the shear band decreases in the same direction, so as to give less localized flow in shear bands. Also, with increasing macroscopic strain, some macroscopic strain hardening is now being observed. This is even stronger under higher triaxiality, $\Sigma_1/\Sigma_2 = 0.73$. However, the rate of void growth is seen from Fig. 12b to be only slightly affected by N and C^R.

6. Hydrostatic stresses in ligament
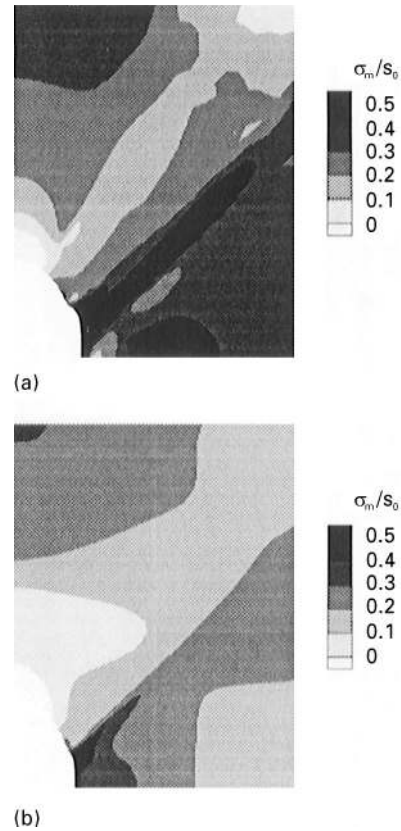Even though the details of craze initiation are not fully established, the value of the hydrostatic (or mean)

Figure 13 Distribution of the hydrostatic mean stress, σ_m, for a material with $N = 6.3$, $C^R = 5.7$ MPa and with the initial void specified by $a_0/b_0 = 0.2$ for low triaxiality loading, $\Sigma_1/\Sigma_2 = 0$, under (a) plane strain, $E_e = 0.14$, and (b) axisymmetric conditions, $E_e = 0.16$.

stress $\sigma_m = 1/3\sigma_{kk}$ plays a crucial role [1, 2, 19]. In view of the importance of the competition between yielding and crazing in the matrix on the fracture toughness of a rubber blend, it is useful therefore to understand the development of hydrostatic stresses in the matrix around a void (as an idealization of a cavitated rubber particle). To fix ideas, let us assume for simplicity that crazing occurs once a critical value of the hydrostatic stress is attained anywhere in the matrix.

It follows immediately from Goodier's [5] elastic analysis for an isolated spherical void, generalized to arbitrary remote stress triaxialities, that the maximum mean stress in the material always occurs at the equator of the void, and can be expressed entirely in terms of Poisson's ratio, ν, and the macroscopic stress parameters Σ_m and Σ_e. Void interaction may enhance this local value, but only by a few per cent for $a_0/b_0 = 0.5$. Once plasticity takes place, the elastic solution loses applicability. On the other hand, for massive plastic deformation in metals, it is known from the work of Bridgman [20] that the hydrostatic stress inside a neck is elevated substantially. Necking of the ligament between voids has also been observed to occur in the foregoing, so that it seems very pertinent to study the evolution of the mean stresses from the early elastic stages until substantial growth of the void and ligament necking.

Figs 13 and 14 show the distribution of the local mean stress, σ_m, at instants (nearly) coinciding with
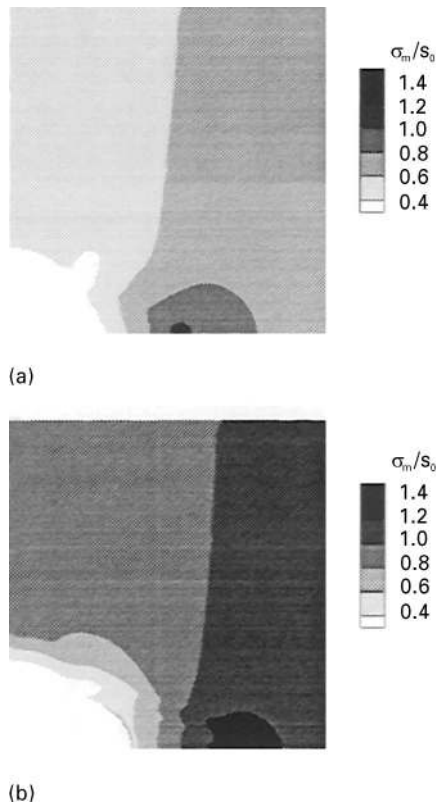
Figure 14 Distribution of the hydrostatic mean stress, σ_m, for the same material as in Fig. 13 but for high triaxiality loading, $\Sigma_1/\Sigma_2 = 0.73$, under (a) plane strain, $E_e = 0.043$, and (b) axisymmetric conditions, $E_e = 0.040$.

Figure 15 Mean stress distributions along the equatorial plane $x_2 = 0$ at different strains E_e for the material shown in Fig. 14 under axisymmetric conditions with $\Sigma_1/\Sigma_2 = 0.73$ for (a) $a_0/b_0 = 0.2$, and (b) $a_0/b_0 = 0.5$. The corresponding stress–strain curves are shown in Figs 6 and 9, respectively.

macroscopic yield under low and high triaxiality, respectively. At those instants, shear bands of various degrees of intensity have already formed, as shown previously in Figs 4 and 5. This and previous plastic flow have, to a large extent, destroyed the elastic mean stress fields, so that the peak values of σ_m are no longer found at the equator of the void but at some distance away from that. This is most clearly seen from Fig. 14 for the higher triaxiality ($\Sigma_1/\Sigma_2 = 0.73$). For the lower triaxiality (Fig. 13a), a peak mean stress is also seen on the equatorial plane away from the void equator, but in this case a band of elevated mean stress is observed as well. This band coincides with the lowest 45° shear bands observed in Fig. 4a which intersects at the void surface with the rather faint dog-ear shape band that is also seen at this point.

Upon closer examination of Fig. 14, along with the plots in Fig. 5, it follows that the locations of the peak hydrostatic stresses practically coincide with the intersection of the currently active shear bands, i.e. the tip of the dog-ear bands. This can be readily understood by noting that, at the tip of crossing shear bands, a state of high dilation must exist for compatibility reasons. Assuming that craze initiation is controlled by the local mean stress, these results suggest that the intersection of shear bands could serve as points of craze initiation, as confirmed by a number of experimental observations, see, for example, [21]. The value of the maximum mean stress in the axisymmetric model is seen to be significantly higher than that in plane strain at roughly the same overall strain. This should
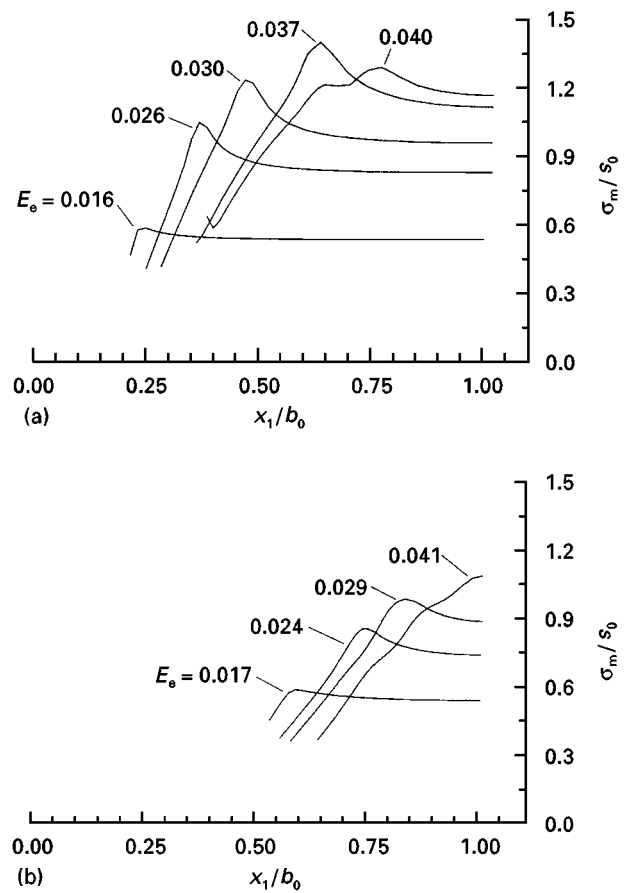
obviously be attributed to the circumferential compatibility conditions that must be met near the intersection of shear bands in addition to the in-plane ones.

To explore further the evolution of the state of hydrostatic stress during the deformation process, Fig. 15 shows the distribution of σ_m over the equatorial plane only, at various stages of the deformation. In this figure, attention is confined to high remote stress triaxiality and to the axisymmetric model, but the results under plane strain have been found to be qualitatively similar. Fig. 15a shows how the stress state shown in Fig. 14b has evolved from the early stages where localized plastic flow had only just initiated near the void equator. Already in those early stages (prior to macroscopic yield), the peak mean stress occurs at some distance ahead of the current void equator, again associated with the intersection of shear bands (cf. Fig. 5b). It is interesting to see that the peak mean stress continuously increases during the stages shown, but reaches a maximum (at $E_e \approx 0.037$) prior to macroscopic yield when the macroscopic mean stress attains a maximum. Also note that this local maximum mean stress σ_m is roughly equal to $1.4s_0$, whereas the maximum macroscopic mean stress Σ_m (at yield) is only $0.86s_0$. Without further exploring the consequences of this, we note that hydrostatic stresses of $1.4s_0$ approach the cavitation instability limit recently established [22] for similar material properties.

3173

Fig. 15b finally illustrates the effect of the relative void size on the local hydrostatic stress development by giving the results for the larger voids, $a_0/b_0 = 0.5$. In the early stages, the mean stresses near the void at corresponding strains are very much similar to that in Fig. 15a for the smaller void. However, at continued straining the location of peak mean stress moves into the ligament regime, and we find the maximum hydrostatic stress at the centre of the ligament, just like in a necked specimen [20]. The maximum value of σ_m found for this larger void is at all stages significantly smaller than for the smaller void. Also we see that the largest peak value is found after macroscopic yield. Assuming that craze initiation is controlled by the value of σ_m this means that for a given value of the critical mean stress, crazing may be initiated in the system with the smaller voids whereas the material with larger voids does not craze.

7. Discussion and conclusions

We have reported the results of detailed finite element studies of the deformations around voids, and their growth, in glassy polymers. The main characteristics of the results are as follows:

1. for stress triaxialities ranging from uniaxial tension to crack-tip like stress states, local plasticity initiates shear bands from the equator of the void before macroscopic yield takes place;
2. with continued macroscopic deformation, these bands develop into one of two types of shear bands occur: wing shaped or dog-ear shaped bands;
3. as these shear bands mature with on-going deformation, they propagate in a direction roughly normal to the band.

In some cases, both families of shear bands occur simultaneously, usually at strains just beyond macroscopic yield. This typically signals a transition from wing-like to dog-ear shaped bands. In these cases, the combined shear band patterns momentarily bear a strong resemblance to the theoretical slip line fields near a rounded notch, as discussed, for example, elsewhere [21, 23]. Such patterns have also been found in a recent numerical study [24] of plasticity around blunt crack tips using the same material model, and similar parameters as used here.

The wing-like shear bands that are predicted under sufficiently low macroscopic stress triaxiality have indeed been observed experimentally by Sue and Yee [8]. They used relatively thick PC plates, containing just a single void, subjected to uniaxial tension; this relates best to our results for the relatively small voids ($a_0/b_0 = 0.2$). Just like in our computations, see Fig. 4a, plasticity was observed to start with a combination of both types of shear bands, followed by strong localization in wing-type bands after macroscopic yield. Unfortunately, the experiments were not continued much beyond yield, so that a comparison of void growth and shear band propagation at the larger strains shown in Fig. 4a is not possible. We are not aware of any similar observations of plastic zones around voids under elevated stress triaxialities, where

we predict dog-ear type shear bands. However, such bands are akin to the main shear bands observed experimentally near the tip of a round notch in a thick PC specimen [25], where it is well-known that the stress triaxiality is raised substantially above the remotely applied state of stress.

When attempting to compare the predicted shear band patterns with experimental observations, care should be taken with the two respective interpretations. In the experiments described elsewhere [8, 25], shear bands are visible through the change in birefringence that has occurred due to molecular reorientation during plasticity. In this paper, what we refer to as shear bands are regions of currently active plasticity; previous plastic deformation does not emerge in the plots. Furthermore, one has to be careful with the size scales. Depending on magnification and material, micrographs often reveal individual microshear bands that are organized in more macroscopic bands. The material model that has been used here is a continuum model, which does not represent individual microshear bands associated with the molecular "shear yielding" process. At best, it provides a continuum representation of such microshear bands in terms of their collective behaviour. Hence, the predicted shear bands should be interpreted as such "macroscopic" bands; the internal structure in terms of micro-shear bands cannot be resolved.

The results presented here supplement the picture that has emerged from earlier studies of voids in elastic–plastic polymeric materials [7–9]. Our analyses differ from the earlier studies in the literature mainly in that (i) proper account has been given of large local strains, and (ii) a physically motivated three-dimensional constitutive description of the elastic–viscoplastic response has been adopted, including strain softening upon yield and subsequent progressive strain hardening. This, together with the fact that today's computer power allows for much finer finite element discretizations, is the reason for the prediction of finer and more pronounced shear bands than earlier ones, e.g. [8–10].

The studies predict a local enhancement of the hydrostatic stress near intersections of shear bands, indicating these as potential locations for craze initiation. The maximum value found anywhere in the ligament between voids tends to increase as the void grows, until macroscopic yield takes place. Depending on the precise craze initiation criterion, this suggests that craze initation need not occur from the void surface, where the elastic stress concentration is, but may await some significant plastic deformation and void growth. This emphasizes that the complex competition between plasticity and crazing in toughening of blends may depend on details of the local plasticity, which is emanable only through computational studies of the present type.

The primary motivation for this study was the local plastic flow around cavitated rubbery particles in amorphous blends. The study is relevant for blends in which the rubber modulus is so low that the stress-carrying capacity of the rubber after cavitation can be neglected, and the cavitated particle can be regarded

as a void. In a follow-up of this work, we will explicitly investigate the role of the rubber, by actually incorporating the rubber particle in the model.

References

1. A. S. ARGON and J. G. HANNOOSH, *Philos. Mag.* **36** (1977) 1195.
2. E. J. KRAMER, "Advances in Polymer Science", Vol. 52/53 (Springer, Berlin, 1983) p. 1.
3. C. B. BUCKNALL, "Toughened Plastics" (Applied Science, London, 1977).
4. A. M. DONALD and E. J. KRAMER, *J. Mater. Sci.* **17** (1982) 1765.
5. J. N. GOODIER, *ASME Appl. Mech. Trans.* **55** (1933) 39.
6. L. J. BROUTMAN and G. PANIZZA, *Int. J. Polym. Mater.* **1** (1971) 95.
7. R. N. HAWARD and D. R. J. OWEN, *J. Mater. Sci.* **8** (1973) 1136.
8. H.-J. SUE and A. F. YEE, *Polymer* **29** (1988) 1619.
9. Y. HUANG and A. J. KINLOCH, *J. Mater. Sci.* **27** (1992) 2753.
10. H.-Y. JEONG and J. PAN, *Int. J. Solids Structures* **32** (1995) 3669.
11. M. C. BOYCE, D. M. PARKS and A. S. ARGON, *Mech. Mater.* **7** (1988) 15.
12. E. M. ARRUDA and M. C. BOYCE, *J. Mech. Phys. Solids* **41** (1993) 389.
13. P. D. WU and E. VAN DER GIESSEN, *ibid.* **41** (1993) 427.
14. E. VAN DER GIESSEN and P. D. WU, in "Mechanics of Plastics and Plastic Composites", edited by M. C. Boyce, MD-Vol. 68/AMD-Vol. 215 (ASME, New York, 1995) p. 203.
15. A. C. STEENBRINK, E. VAN DER GIESSEN and P. D. WU, *J. Mech. Phys. Solids* **45** (1997) 405.
16. R. N. HAWARD and G. THACKRAY, *Proc. R. Soc. Lond.* **A302** (1968) 453.
17. A. S. ARGON, *Philos. Mag.* **28** (1973) 839.
18. P. D. WU and E. VAN DER GIESSEN, *Eur. J. Mech. A/Solids* **15** (1996) 799.
19. M. E. J. DEKKERS and D. HEIKENS, *J. Mater. Sci.* **18** (1983) 3281.
20. P. W. BRIDGMAN, "Studies in Large Plastic Flow and Fracture" (McGraw-Hill, New York, 1952).
21. I. NARISAWA, M. ISHIKAWA and H. OGAWA, *J. Mater. Sci.* **15** (1980) 2059.
22. A. C. STEENBRINK and E. VAN DER GIESSEN, Delft University of Technology, LTM Report 1118 (1996).
23. H.-Y. JEONG, X.-W. LI, A. F. YEE and J. PAN, *Mech. Mater.* **19** (1994) 29.
24. J. LAI and E. VAN DER GIESSEN, Delft University Technology Report LTM 1105 (1996).
25. I. NARISAWA and A. F. YEE, in "Materials Science and Technology: A Comprehensive Treatment", edited by E. L. Thomas, Vol. 121, "Structure and Properties of Polymers" (VCH, Weinheim, New York, 1993) p. 699.